

# The onset of energetic particle irradiation in Class 0 protostars<sup>★</sup>

C. Favre<sup>1,2</sup>, A. López-Sepulcre<sup>3</sup>, C. Ceccarelli<sup>1,2</sup>, C. Dominik<sup>4</sup>, P. Caselli<sup>5</sup>, E. Caux<sup>6,7</sup>, A. Fuente<sup>8</sup>, M. Kama<sup>9</sup>, J. Le Bourlot<sup>10</sup>, B. Lefloch<sup>1,2</sup>, D. Lis<sup>10,11</sup>, T. Montmerle<sup>12</sup>, M. Padovani<sup>13</sup>, and C. Vastel<sup>6,7</sup>

<sup>1</sup> Univ. Grenoble Alpes, IPAG, F-38000 Grenoble, France

<sup>2</sup> CNRS, IPAG, F-38000 Grenoble, France

e-mail: [cecile.favre@univ-grenoble-alpes.fr](mailto:cecile.favre@univ-grenoble-alpes.fr)

<sup>3</sup> Institut de Radioastronomie Millimétrique, 300 rue de la Piscine, F-38406 Saint Martin d'Hères, France.

<sup>4</sup> Astronomical Institute "Anton Pannekoek", University of Amsterdam, Kruislaan 403, NL-1098SJ Amsterdam, Netherlands

<sup>5</sup> Max-Planck-Institute for Extraterrestrial Physics (MPE), Giessenbachstr. 1, 85748 Garching, Germany

<sup>6</sup> Université de Toulouse, UPS-OMP, IRAP, Toulouse, France

<sup>7</sup> CNRS, IRAP, 9 Av. colonel Roche, BP 44346, 31028, Toulouse Cedex 4, France

<sup>8</sup> Observatorio Astronómico Nacional (OAN, IGN), Apdo 112, 28803 Alcalá de Henares, Spain

<sup>9</sup> Leiden Observatory, P.O. Box 9513, NL-2300 RA, Leiden, The Netherlands

<sup>10</sup> LERMA, Observatoire de Paris, PSL Research University, CNRS, Sorbonne Universités, UPMC Univ. Paris 06, F-75014, Paris, France

<sup>11</sup> Cahill Center for Astronomy and Astrophysics 301-17, California Institute of Technology, Pasadena, CA 91125, USA

<sup>12</sup> Institut d'Astrophysique de Paris, 98bis Bd Arago, 75014 Paris, France

<sup>13</sup> INAF-Osservatorio Astrofisico di Arcetri, Largo E. Fermi, 5 – 50125 Firenze, Italy

Received September 15, 1996; accepted March 16, 1997

## ABSTRACT

**Context.** The early stages of low-mass star formation are likely to be subject to intense ionization by protostellar energetic MeV particles. As a result, the surrounding gas is enriched in molecular ions, such as  $\text{HCO}^+$  and  $\text{N}_2\text{H}^+$ . Nonetheless, this phenomenon remains poorly understood for Class 0 objects. Recently, based on Herschel observations taken as part of the key program Chemical HErschel Surveys of Star forming regions (CHESS), a very low  $\text{HCO}^+/\text{N}_2\text{H}^+$  abundance ratio of about 3-4, has been reported toward the protocluster OMC-2 FIR4. This finding suggests a cosmic-ray ionization rate in excess of  $10^{-14} \text{ s}^{-1}$ , much higher than the canonical value of  $\zeta = 3 \times 10^{-17} \text{ s}^{-1}$  (value expected in quiescent dense clouds).

**Aims.** To assess the specificity of OMC-2 FIR4, we have extended this study to a sample of sources in low- and intermediate mass. More specifically, we seek to measure the  $\text{HCO}^+/\text{N}_2\text{H}^+$  abundance ratio from high energy lines ( $J \geq 6$ ) toward this source sample in order to infer the flux of energetic particles in the warm and dense gas surrounding the protostars.

**Methods.** We use observations performed with the Heterodyne Instrument for the Far-Infrared spectrometer on board the Herschel Space Observatory toward a sample of 9 protostars.

**Results.** We report  $\text{HCO}^+/\text{N}_2\text{H}^+$  abundance ratios in the range of 5 up to 73 toward our source sample. The large error bars do not allow us to conclude whether OMC-2 FIR4 is a peculiar source. Nonetheless, an important result is that the measured  $\text{HCO}^+/\text{N}_2\text{H}^+$  ratio does not vary with the source luminosity. At the present time, OMC-2 FIR4 remains the only source where a high flux of energetic particles is clearly evident. More sensitive and higher angular resolution observations are required to further investigate this process.

**Key words.** stars: formation – stars: protostars – ISM: molecules – ISM: cosmic rays

## 1. Introduction

Meteoritic materials conserve the traces of a violent past of the early Solar System history. Specifically, the derived overabundance of short-lived radionuclides (SLRs) like  $^{10}\text{Be}$  provides evidence for a strong irradiation ( $\sim 10^{19} - 10^{20}$  protons  $\text{cm}^{-2}$  in units of fluence) by energetic ( $\geq 10 - 20$  MeV) particles (e.g. Gounelle et al. 2013). Various theories have been evoked in the literature to explain the origin of this energetic particle irradiation: a) galactic cosmic rays anchored to the Solar prestellar clump magnetic field and focused in the Solar Nebula (e.g. Desch et al. 2004), b) particles accelerated in the atmosphere of the young Sun (Bricker & Caffee 2010), c) particles

accelerated at the X-wind intersection (e.g. Gounelle et al. 2006, 2013), and, finally, d) particles accelerated in a dense supersonic protostellar jet (Padovani et al. 2015, 2016).

Unfortunately, it is difficult to distinguish between the above theories, since the irradiation period that happened in our own Solar System is over. If we could observe the process today in forming Sun-like stars, then we might have more constraints to understand what happened to our Solar System. To this end, we would need to discover protostellar sources with signatures of energetic particle irradiation. Unfortunately, the direct detection of these energetic particles is impossible. The problem is similar to that of detecting the sources of acceleration of cosmic rays, as the latter are scattered by the galactic magnetic fields and, consequently, have lost the memory of their origin when they arrive on Earth. As in the cosmic ray case, a way forward is to look for signatures of the interaction of the energetic particles with the

<sup>★</sup> *Herschel* is an ESA space observatory with science instruments provided by European-led Principal Investigator consortia and with important participation from NASA.

Table 1. Selected sources.

Source	R.A. (J2000)	Dec. (J2000)	D (pc)	$L_{\text{bol}} (L_{\odot})$	$v_{\text{LSR}} (\text{km s}^{-1})$	Ref	Herschel OBSIDs	
							Low-mass	Intermediate-mass
VLA1623	16 26 26.4	-24 24 30.0	120	1	3.8	1, 2, 3	1342249850, 1342250201, 1342250476, 1342250715, 1342250733, 1342251210, 1342251211, 1342251248 and 1342251504	
L1527	04 39 53.9	+26 03 10.0	140	2	5.9	4, 5, 6	1342249400, 1342249416, 1342249434, 1342249435, 1342249615, 342249616, 342249861, 1342250193 and 1342250194	
L1157-MM	20 39 06.2	+68 02 22.0	325	11	2.6	5, 6, 7, 8, 9	1342245336, 1342246461, 1342246462, 1342246499, 1342245998, 1342245999, 1342246075 and 1342247020	
NGC1333-IRAS2	03 28 55.4	+31 14 35.0	220	16	7.45	10, 11	1342248525, 1342248896, 1342248912, 1342248913, 1342249430, 1342249431, 1342249604 and 1342249606	
Intermediate-mass								
Serpens-FIRS 1	18 29 49.6	+01 15 20.6	230	33	8	12, 13	1342243674, 1342251636, 1342251637, 1342253636, 1342253795, 1342254436, 1342254437 and 1342268145	
L1641 S3 MMS 1	05 39 55.9	-07 30 28.0	500	67	5	13	1342249619, 1342249863, 1342250183, 1342250184, 1342250679, 1342251109, 1342251207, 1342251208 and 1342251507	
Cep E-mm	23 03 13.1	+61 42 26.0	730	100	-11	6, 12, 13	1342246466, 1342246467, 1342246009, 1342246010, 1342246065, 1342246074, 1342246333, 1342246337 and 1342247171	
IC1396N	21 40 41.7	+58 16 12.8	750	150	0.5	12, 13	1342245332, 1342245333, 1342245587, 1342246002, 1342246003, 1342246464, 1342246465, 1342247022 and 1342247174	
NGC7129-FIRS2	21 43 01.7	+66 03 23.6	1250	500	-10	12, 13	1342243672, 1342245334, 1342245335, 1342246468, 1342246469, 1342246000, 1342246001, 1342246001 and 1342247039	

**References.** (1) Andre et al. (1993) (2) Loinard et al. (2008) (3) Maury et al. (2012) (4) Karska et al. (2013) (5) Kristensen et al. (2012) (6) López-Sepulcre et al. (2015) (7) Straizys et al. (1992) (8) Giannini et al. (2001) (9) Jørgensen et al. (2007) (10) Jørgensen et al. (2004) (11) Cernis (1990) (12) Crimier et al. (2010) (13) Alonso-Albi et al. (2010).

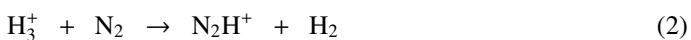
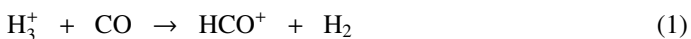
**Table 2.** Spectroscopic line parameters.

Molecule	Transition	Frequency (MHz)	$E_{\text{up}}$ (K)	$S\mu^2$ (D <sup>2</sup> )
HCO <sup>+</sup>	6–5	535061.581	89.9	91.3
HCO <sup>+</sup>	8–7	713341.228	154.1	121.7
HCO <sup>+</sup>	11–10	980636.494	282.4	167.3
HCO <sup>+</sup>	12–11	1069693.891	333.8	182.5
H <sup>13</sup> CO <sup>+</sup>	6–5	520459.884	87.4	91.3
H <sup>13</sup> CO <sup>+</sup>	7–6	607174.646	116.6	106.5
H <sup>13</sup> CO <sup>+</sup>	9–8	780562.812	187.3	136.9
N <sub>2</sub> H <sup>+</sup>	6–5	558966.503	93.9	624.3
N <sub>2</sub> H <sup>+</sup>	8–7	745209.868	160.9	832.3
N <sub>2</sub> H <sup>+</sup>	11–10	1024443.025	295.1	1144.3

**Notes.** We used the spectroscopic data parameters from Davies & Rothwell (1984), Kawaguchi et al. (1985), Hirota & Endo (1988), Botschwina et al. (1993), Lattanzi et al. (2007) and Tinti et al. (2007) for HCO<sup>+</sup>, from Gregersen & Evans (2001), Schmid-Burgk et al. (2004) and Lattanzi et al. (2007) for H<sup>13</sup>CO<sup>+</sup> and, from Verhoeve et al. (1990), Havenith et al. (1990), Caselli et al. (1995), Amano et al. (2005) and Pagani et al. (2009) for N<sub>2</sub>H<sup>+</sup>. Note that all spectroscopic data are available from the Cologne Database for Molecular Spectroscopy molecular line catalog (CDMS, Müller et al. 2005) at Splatalogue (<http://www.splatalogue.net>, Remijan et al. 2007).

immediate surrounding material. It turns out that two effects are, in principle, observable: i) an enhanced  $\gamma$ -ray emission, caused by the interaction of  $\geq 280$  MeV protons with the H-atoms (e.g. Hayakawa 1952; Stecker et al. 1971) and, ii) an enhanced ionization fraction, caused by the interaction of 0.1 – 1 GeV particles (e.g. Indriolo et al. 2010; Ceccarelli et al. 2011).

In practice, however, for sensitivity reasons, only the second effect is observable in protostars. Also, since the source emitting the energetic particles is, supposedly, embedded in the accreting envelope, one needs to measure the ionization of the gas close to it, namely in the inner warm and dense regions. One way to do it, is to observe ions that have directly or indirectly been created by the energetic particles, with relatively high upper level energy transitions, in order to probe the dense and warm gas. Two ions satisfy these two criteria: HCO<sup>+</sup> and N<sub>2</sub>H<sup>+</sup>. Indeed, both possess rotational transitions in the sub-millimeter with the appropriate upper level energies ( $\geq 100$  K), and they are created by the reaction of H<sub>3</sub><sup>+</sup> (an ion that is almost directly created by the energetic particles or X-ray induced secondary electrons) with CO and N<sub>2</sub>, respectively:



A first observation of the high lying transitions (with  $J \geq 6$ , namely upper level energy  $\geq 100$  K) of HCO<sup>+</sup> and N<sub>2</sub>H<sup>+</sup> was obtained by Ceccarelli et al. (2014) toward the protocluster OMC-2 FIR4 (Shimajiri et al. 2008; López-Sepulcre et al. 2013) by HSO (*Herschel Space Observatory*) within the Key Project CHESS (Ceccarelli et al. 2010). Unexpectedly, the derived HCO<sup>+</sup>/N<sub>2</sub>H<sup>+</sup> abundance ratio turned out to be very low, 3–4, when compared to that of gas in “standard” conditions ( $\gg 10$ , e.g. Sanhueza et al. 2012; Hoq et al. 2013). When considering the formation (Eqs. (1) and (2)) and destruction routes of both molecules, it turns out that the only way to obtain such a low HCO<sup>+</sup>/N<sub>2</sub>H<sup>+</sup> abundance ratio is when both molecules are destroyed by electrons, which can only happen when the gas ionization is dominated by i) energetic particles (which is the case of OMC-2 FIR4, see Ceccarelli et al. 2014) or ii) X-ray irradiation (Stäuber et al. 2005), both of which interact with atomic and molecular hydrogen to produce H<sub>3</sub><sup>+</sup> and electrons. Alternatively,

a low HCO<sup>+</sup>/N<sub>2</sub>H<sup>+</sup> abundance ratio can be a result of the depletion of gaseous CO with respect to N<sub>2</sub> due to the CO freeze-out. Indeed, the CO gas-phase depletion by adsorption onto grains mantles would then decrease the HCO<sup>+</sup> abundance, and likely enhance that of N<sub>2</sub>H<sup>+</sup> (see Section 5). However, this occurs only in cold ( $\leq 20$ –25 K) material, which is not the case in OMC-2 FIR4, since the temperature probed by the  $J \geq 6$  transitions is  $\geq 30$  K. Finally, a high abundance of water could also destroy HCO<sup>+</sup> and N<sub>2</sub>H<sup>+</sup> (e.g. Stäuber et al. 2006) so that their ratio might decrease (see also Ceccarelli et al. 2014). Again, in the case of OMC-2 FIR4, the observed water abundance is too low for this explanation to be valid. Therefore, the observed low ratio can only be explained by the presence of one or more embedded sources emitting a large flux of energetic particles. Furthermore, the derived dose of energetic particles is similar to that experienced by the young Solar System (for further details, see Ceccarelli et al. 2014).

These findings lead one to ask whether OMC-2 FIR4 is a peculiar source or if other protostars do experience the same process. If the latter, what does the process depend on: age, luminosity, mass or multiplicity? In order to address the above questions, we followed up with a survey of the high- $J$  HCO<sup>+</sup> and N<sub>2</sub>H<sup>+</sup> HSO observations toward a sample of low- and intermediate-mass embedded protostars. In Section 2, we present the observations. Results are presented and discussed in Sections 3, 4 and 5, with conclusions set out in Section 6.

## 2. Observations and data reduction

### 2.1. Source sample

Our survey is composed of a sample of nine well-known low- and intermediate- mass embedded protostars that are listed in Table 1 along with their respective coordinates, distances from the Sun, luminosities and LSR velocities. The sources were selected in order to cover a wide range of luminosities, from 1 L<sub>⊙</sub> up to 500 L<sub>⊙</sub> (see Table 1), and consequently, likely masses and evolutionary stages.

### 2.2. Observed frequencies

As we aimed to derive accurate HCO<sup>+</sup>/N<sub>2</sub>H<sup>+</sup> abundance ratios toward the inner dense and warm region of the envelope surrounding the target sources, high transitions ( $6 \leq J \leq 12$ ) of

$\text{HCO}^+$  and  $\text{N}_2\text{H}^+$  were selected. Furthermore,  $\text{H}^{13}\text{CO}^+$  observations were performed to evaluate  $\text{HCO}^+$  optical depth. The observed  $\text{HCO}^+$ ,  $\text{H}^{13}\text{CO}^+$  and  $\text{N}_2\text{H}^+$  frequencies are listed in Table 2 together with the spectroscopic line parameters. Observations of all the targeted lines (see Table 2) have been performed toward our source sample, except for the  $\text{HCO}^+$  (12–11) transition, which has not been observed toward the following objects: NGC1333–IRAS2, Serpens–FIRS 1 and NGC7129–FIRS2.

### 2.3. Herschel HIFI observations

The observations were performed with the Heterodyne Instrument for the Far–Infrared (HIFI) spectrometer (de Graauw et al. 2010) on board the Herschel Space Observatory (Pilbratt et al. 2010) between 2012 April and August as part of a Herschel Open Time. The data were obtained in fast chop dual beam switch (DBS program) mode pointed toward our sources (see coordinates in Table 1) at a spectral resolution of 1.1 MHz. The HPBW lies in the range  $18''$  up to  $41''$  (at 1.2 THz and 535 GHz, respectively).

Data were exported to CLASS90 that is part of the GILDAS software<sup>1</sup> for reduction and analysis purposes. Calibration uncertainties are estimated to be less than 15% (Roelfsema et al. 2012). The continuum emission was fitted using a first–order polynomial and then subtracted from the scans. Then, the spectra that are reported in this study were – for each source and each targeted line – obtained after "stitching" data from each scan. Also, noting that the line–widths of the observed lines are in the range of  $1\text{--}4\text{ km s}^{-1}$  (see Section 3), the spectra were smoothed to a spectral resolution of 2.2 MHz. Finally, spectra that are shown in this paper are in units of the main beam temperature ( $T_{\text{MB}}$ ). The intensity conversion from antenna temperature ( $T_{\text{A}}^*$ ) to main beam temperature was done using the efficiencies (which include the frequency dependency) given by Michael Mueller and Willem Jellema (2014).<sup>2</sup>

## 3. Results

In the following (sub)sections, we present and describe in detail the results that were obtained with the HSO/HIFI data.

### 3.1. Spectra

Figures 1 and 2 show the respective spectra of the  $\text{HCO}^+$ ,  $\text{H}^{13}\text{CO}^+$  and  $\text{N}_2\text{H}^+$  transitions (see Table 2) observed with Herschel toward the Serpens–FIRS 1 and IC1396N protostars and, Figures A.1 to A.7, in Appendix A, display the spectra of the other observed sources. For display purposes, the spectra have been smoothed to a spectral resolution of 4.4 MHz. The bulk of the molecular emission appears to peak close to the systemic velocity of the targeted sources (see Table 1). The observed line parameters of the  $\text{HCO}^+$ ,  $\text{H}^{13}\text{CO}^+$  and  $\text{N}_2\text{H}^+$  transitions toward our survey are summarized in Tables B.1 to B.9, in Appendix B. In the following analysis, we assume that the molecular emission line is *i*) clearly detected if the peak intensity is greater than  $3\sigma$  and the integrated intensity,  $\int T_{\text{MB}}dV$ , is greater than  $5\sigma$ , *ii*) "weakly" detected if the peak intensity is lower than the  $3\sigma$  level but  $\int T_{\text{MB}}dV \geq 5\sigma$  and, *iii*) tentatively detected if both the peak intensity and  $\int T_{\text{MB}}dV$  are at the  $3\sigma$  level. The measured inte-

grated line intensities of  $\text{HCO}^+$ ,  $\text{H}^{13}\text{CO}^+$  and  $\text{N}_2\text{H}^+$  in all the sources are listed in Table 3.

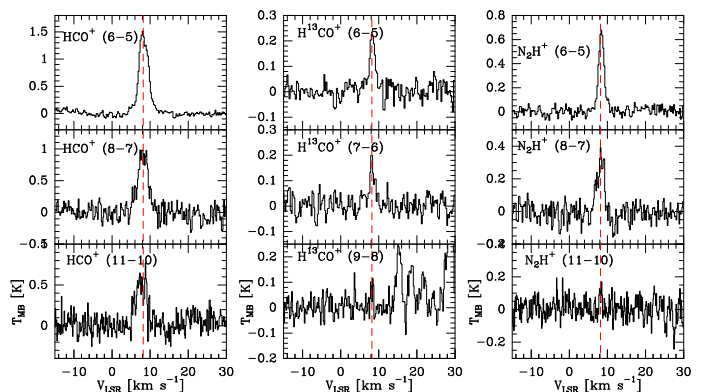


**Fig. 1.** Spectra observed toward Serpens–FIRS 1. Dashed red lines indicate a  $v_{\text{LSR}} = 8.2\text{ km s}^{-1}$ . The name of the observed transition is indicated on each plot.

#### 3.1.1. $\text{HCO}^+$

All the targeted  $\text{HCO}^+$  transitions (see Table 2) are detected toward Serpens–FIRS 1, IC1396N, NGC1333–IRAS2, L1641 S3 MMS 1 and NGC7129–FIRS2. We note that the  $\text{HCO}^+$  (6–5) transition is the only one detected toward L1527 and L157–MM. Finally, we only report a detection of the  $\text{HCO}^+$  (12–11) transitions in direction of the sources L1641 S3 MMS 1 and IC1396N. Incidentally, it is important to note that the line profile of  $\text{HCO}^+$  (6–5) appears broadened (e.g., see, Fig. 2 toward IC1396N) by emission from different components within the Herschel beam. In this study, we only focus on the emission arising from the inner dense and warm region of the envelopes surrounding our source sample. We have therefore decomposed the observed profiles into two Gaussians: a broad one and a narrow one. More specifically, we only analyse the emitting gas from the region/component in which we assume that  $\text{HCO}^+$  and  $\text{N}_2\text{H}^+$  are both co-spatial, namely on the narrow component. Therefore, the present study only reports in its Tables and Figures, the parameters associated with this region.

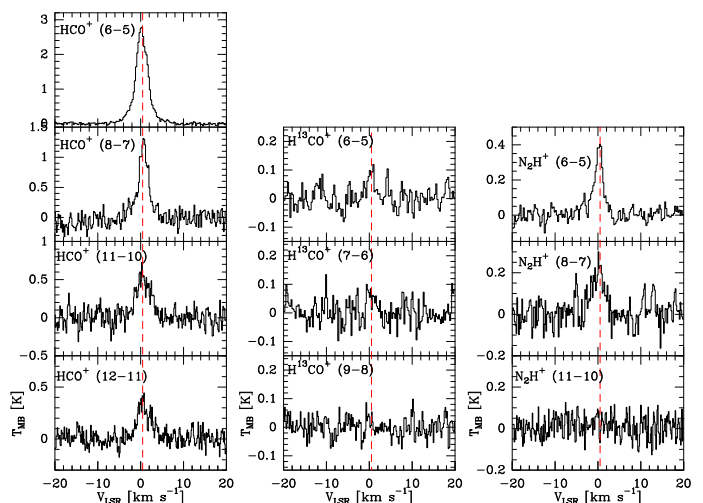


**Fig. 2.** Spectra observed toward IC1396N. Dashed red lines indicate a  $v_{\text{LSR}} = 0.5\text{ km s}^{-1}$ . The name of the observed transition is indicated on each plot.

<sup>1</sup> <http://www.iram.fr/IRAMFR/GILDAS/>

<sup>2</sup> see [http://herschel.esac.esa.int/twiki/pub/Public/HifiCalibrationWeb/HifiBeamReleaseNote\\_Sep2014.pdf](http://herschel.esac.esa.int/twiki/pub/Public/HifiCalibrationWeb/HifiBeamReleaseNote_Sep2014.pdf).

**Table 3.** Integrated line intensities of  $\text{HCO}^+$ ,  $\text{H}^{13}\text{CO}^+$  and  $\text{N}_2\text{H}^+$  toward our source sample.

Source	$\int T_{\text{MB}} dV \text{ (K km s}^{-1}\text{)}$										
	$\text{HCO}^+$			$\text{H}^{13}\text{CO}^+$			$\text{N}_2\text{H}^+$				
	(6–5)	(8–7)	(11–10)	(12–11)	(6–5)	(7–8)	(9–8)	(6–5)	(8–7)	(11–10)	
VLA1623	2.2(0.4)	0.7(0.2)	$\leq 0.5$	$\leq 0.3$	0.10(0.06)	$\leq 0.2$	$\leq 0.3$	0.16(0.06)	$\leq 0.3$	$\leq 0.2$	
L1527	1.26(0.09)	$\leq 0.8$	$\leq 1.0$	$\leq 0.6$	$\leq 0.3$	$\leq 0.4$	$\leq 0.3$	$\leq 0.3$	$\leq 0.5$	$\leq 0.4$	
L1157-MM	0.63(0.09)	$\leq 0.8$	$\leq 0.8$	$\leq 0.5$	$\leq 0.2$	$\leq 0.3$	$\leq 0.2$	$\leq 0.2$	$\leq 0.4$	$\leq 0.3$	
NGC1333-IRAS2	1.4(0.6)	1.5(0.3)	0.8(0.3)	–	0.09(0.06)	$\leq 0.1$	$\leq 0.1$	0.36(0.09)	$\leq 0.6$	$\leq 0.6$	
Serpens-FIRS 1	3.8(0.6)	3.2(0.3)	1.9(0.3)	–	0.41(0.09)	0.29(0.09)	0.08(0.06)	1.21(0.09)	0.7(0.1)	0.10(0.08)	
L1641 S3 MMS 1	0.9(0.4)	1.5(0.3)	1.6(0.3)	1.0(0.3)	$\leq 0.2$	$\leq 0.1$	$\leq 0.1$	0.18(0.09)	$\leq 0.3$	$\leq 0.2$	
Cep E-mm	1.9(0.2)	1.3(0.4)	0.3(0.2)	$\leq 0.9$	$\leq 0.2$	$\leq 0.2$	$\leq 0.2$	0.11(0.06)	$\leq 0.3$	$\leq 0.2$	
IC1396N	6.7(0.6)	3.4(0.5)	2.24(0.05)	1.31(0.03)	0.21(0.10)	0.2(0.1)	$\leq 0.4$	0.9(0.1)	0.8(0.2)	$\leq 0.6$	
NGC7129-FIRS2	1.2(0.2)	1.6(0.4)	0.5(0.3)	–	$\leq 0.5$	$\leq 0.5$	$\leq 0.4$	0.34(0.09)	$\leq 0.6$	$\leq 0.4$	

**Notes.** For further details, see Tables B.1 to B.9 in Appendix B. The  $3\sigma$  uncertainties that are given in brackets result from gaussian fits performed with the CLASS software. Finally, note that the  $\text{HCO}^+$  (12–11) transition has not been observed toward NGC1333-IRAS2, Serpens-FIRS 1 and NGC7129-FIRS2 (see Sec. 2.2).

**Table 4.** Beam dilution factor.

Source	D (pc)	Beam dilution factor, B			
		HCO <sup>+</sup> (6–5)	HCO <sup>+</sup> (8–7)	HCO <sup>+</sup> (11–10)	HCO <sup>+</sup> (12–11)
VLA1623	120	0.82	0.89	0.94	0.95
L1527	140	0.77	0.86	0.92	0.93
L1157–MM	325	0.39	0.52	0.68	0.72
NGC1333–IRAS2	220	0.58	0.71	0.82	0.85
Serpens–FIRS 1	230	0.56	0.69	0.81	0.83
L1641 S3 MMS 1	500	0.21	0.32	0.47	0.52
Cep E–mm	730	0.11	0.18	0.29	0.33
IC1396N	750	0.11	0.17	0.28	0.32
NGC7129–FIRS2	1250	0.04	0.07	0.12	0.15

### 3.1.2. H<sup>13</sup>CO<sup>+</sup>

The H<sup>13</sup>CO<sup>+</sup> (6–5) transition is detected toward the Serpens–FIRS 1, IC1396N, VLA1623 and NGC1333–IRAS2 sources. In addition, we report a detection and tentative detection of H<sup>13</sup>CO<sup>+</sup> (7–6) in the direction of the Serpens–FIRS 1 and IC1396N intermediate–mass protostars, respectively. Incidentally, we tentatively detect H<sup>13</sup>CO<sup>+</sup> (9–8) toward Serpens–FIRS 1. Finally, we do not detect H<sup>13</sup>CO<sup>+</sup> toward the following 5 sources: L1527, L1157–MM, L1641 S3 MMS 1, Cep E–mm and NGC7129–FIRS2.

### 3.1.3. N<sub>2</sub>H<sup>+</sup>

The N<sub>2</sub>H<sup>+</sup> (6–5) transition is detected toward the following 6 protostars: Serpens–FIRS 1, IC1396N, VLA1623, NGC1333–IRAS2, L1641 S3 MMS 1 and NGC7129–FIRS2 and tentatively detected toward Cep E–mm. We also report the detection of N<sub>2</sub>H<sup>+</sup> (8–7) in the direction of Serpens–FIRS 1 and IC1396N. The N<sub>2</sub>H<sup>+</sup> (11–10) is tentatively detected toward Serpens–FIRS 1. However, we do not detect N<sub>2</sub>H<sup>+</sup> toward either L1527 and L1157–MM.

To summarize, the main observational results (see Table 3), are as follows:

- The four HCO<sup>+</sup> transitions have been detected in the majority of the sources, with the lowest transition,  $J = 6 - 5$ , detected in all of them.
- On the contrary, the H<sup>13</sup>CO<sup>+</sup> lines are mostly undetected, with even the  $J = 6 - 5$  line detected in only four out of the nine sources.
- Finally, the N<sub>2</sub>H<sup>+</sup>  $J = 6 - 5$  line was detected in seven out of the nine sources and the  $J = 8 - 7$  in only two of them.

## 3.2. Spectral Line Energy Distribution (SLED) of HCO<sup>+</sup>

The sources observed in the present study lie at different distance from the Sun (see Table 1). Beam dilution not only depends on the source size of the emitting region but in addition depends on the distance of the source. Under the assumption of an emitting region of 0.05 pc for each source, we can define the beam dilution factor,  $B$ , as follows (Goldsmith & Langer 1999):

$$B = \frac{(0.05/d)^2}{(\theta_b)^2 + (0.05/d)^2}, \quad (3)$$

where  $d$  is the distance from the Sun (pc) and  $\theta_b$  the Herschel beam (″), respectively. For each source, the respective derived  $B$  factor (see Table 4) is used to correct for beam dilution the integrated line intensity of the HCO<sup>+</sup> lines.

Figure 3 shows the observed Spectral Line Energy Distribution (SLED) of HCO<sup>+</sup>, corrected for beam dilution, as a function of the upper  $J$  transition toward all sources. Table 5 gives the measured integrated line intensity ratios, HCO<sup>+</sup> (6–5) / HCO<sup>+</sup> (8–7), toward our survey. It is immediately apparent that the HCO<sup>+</sup> (6–5)/(8–7) line ratio suggests two classes of sources. Indeed, in VLA1623, IC1396N and perhaps Cep E–mm, this ratio is about 3, whereas it is closer to unity (within the error bars) toward the other sources. This finding strongly suggests that the gas is warmer and denser in the latter group of sources. Nonetheless, a caveat of this approach is related to the opacities of the HCO<sup>+</sup> (8–7) lines. Here, we assume that the emission is optically thin. However, if  $\tau_{\text{HCO}^+(8-7)} \gg 1$ , the gas probed toward VLA1623 and IC1396N could be warmer.

Unfortunately, given the reduced number of detected lines in each source, we could not carry out a LVG analysis to constrain the density and temperature of the emitting gas, as was done in Ceccarelli et al. (2014) for OMC-2 FIR4.

**Table 5.** Measured integrated line intensity HCO<sup>+</sup> (6–5) / HCO<sup>+</sup> (8–7) ratios toward our source sample.

Source	HCO <sup>+</sup> (6–5) / HCO <sup>+</sup> (8–7)
VLA1623	3.4(1.2)
L1527	>1.8
L1157–MM	> 1.1
NGC1333–IRAS2	1.1(0.5)
Serpens–FIRS 1	1.5(0.3)
L1641 S3 MMS 1	0.9(0.4)
Cep E–mm	2.4(0.8)
IC1396N	3.0(0.5)
NGC7129–FIRS2	1.3(0.4)

## 4. HCO<sup>+</sup>/N<sub>2</sub>H<sup>+</sup> abundance ratio determination

As explained in the Introduction, the goal of this article is to measure the HCO<sup>+</sup>/N<sub>2</sub>H<sup>+</sup> abundance ratio toward our sample of low-mass and intermediate–mass sources in order to infer the flux of energetic particles in the interior of the protostar envelopes. To derive this ratio, we used the integrated line intensity ratio of the HCO<sup>+</sup> (6–5) and N<sub>2</sub>H<sup>+</sup> (6–5) lines, which are the main lines detected in the majority of the sources (see Table 3). This approach relies on the assumption that HCO<sup>+</sup> emits from the same region as N<sub>2</sub>H<sup>+</sup>. As these ( $J = 6 - 5$ ) transitions probe warm and dense gas and are chemically similar, this assumption is likely correct. More specifically, in the following sections, we obtain a robust estimate from the HCO<sup>+</sup> (6–5) over N<sub>2</sub>H<sup>+</sup> (6–5) line intensity ratio toward each observed source. In addition, it

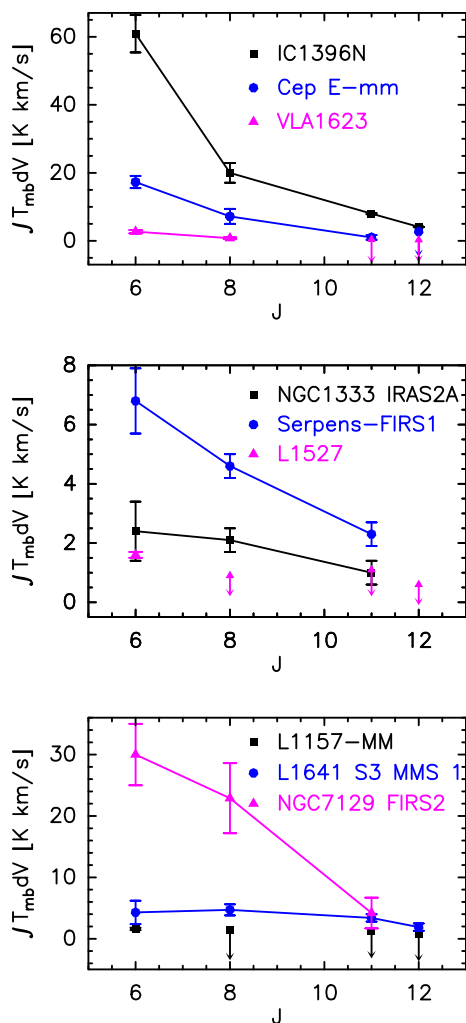


**Fig. 3.** SLED of  $\text{HCO}^+$  as a function of the upper  $J$  transition toward the observed sources (see Table 1). The name of the source is indicated in each panel.

is important to note that the measured integrated line intensity ratios do not suffer from beam dilution effect because the two targeted transitions have similar line frequencies and have been observed within the same beam. Thus, since the two transitions have similar critical density and upper level energy (see Table 2), the intensity ratio conversion to an abundance ratio only assumes that the two species are co-existing in the telescope beam, once the ratio is corrected for the line opacity (see below). As a consequence, the obtained ratio represents an upper limit to the lowest  $\text{HCO}^+/\text{N}_2\text{H}^+$  abundance ratio in the region.

#### 4.1. Line opacity

As stated above, the  $\text{HCO}^+$  abundance relative to  $\text{N}_2\text{H}^+$  depends on the optical depth. The observations of the  $\text{H}^{13}\text{CO}^+$  lines, allow us to estimate the optical depth of the  $\text{HCO}^+$  lines. To this end, we compare the integrated intensity of  $\text{HCO}^+$  (6–5) to that of  $\text{H}^{13}\text{CO}^+$  (6–5), when available (see Section 3.1.2 and Tables 3, and B.1 to B.9). From that, we estimate a flux ratio of 22, 16, 9 and 32 toward the VLA1623, NGC1333–IRAS2, Serpens–FIRS 1 and IC1396N protostars, respectively. Thus, if we assume an isotopic ratio of  $^{12}\text{C}/^{13}\text{C}=68$  for the local ISM (see Milam et al. 2005), the  $\text{HCO}^+$  (6–5) line is optically thick in all these sources, with  $\tau$  lying in the range  $\sim 2$  up to 8 (see Table 6).

Regarding  $\text{N}_2\text{H}^+$ , it is important to state that our analysis hinges upon the assumption that the  $\text{N}_2\text{H}^+$  (6–5) emission is optically thin. However, if  $\tau_{\text{N}_2\text{H}^+} \gg 1$ , the derived  $\text{HCO}^+/\text{N}_2\text{H}^+$  abundance ratio should be an upper limit for the true  $\text{HCO}^+/\text{N}_2\text{H}^+$  abundance. In that instance, the true  $\text{HCO}^+/\text{N}_2\text{H}^+$  ratio would be smaller than the one reported in our study.

**Table 6.** Measured integrated line intensity  $\text{HCO}^+$  (6–5) /  $\text{N}_2\text{H}^+$  (6–5) ratios toward our source sample.

Source	$\tau_{\text{HCO}^+}$	$\text{HCO}^+$ (6–5) / $\text{N}_2\text{H}^+$ (6–5)
VLA1623	3.1	42.5(30.1)
L1527	–	>4
L1157–MM	–	>3
NGC1333–IRAS2	4.5	17.0(12.1)
Serpens–FIRS 1	9.2	23.0(5.3)
L1641 S3 MMS 1	–	>5, <76
Cep E–mm	–	>17, <124
IC1396N	2.9	15.9(7.8)
NGC7129–FIRS2	–	>4, <100

#### 4.2. $\text{HCO}^+/\text{N}_2\text{H}^+$ abundance ratio

Figure 4 shows the distribution of the  $\text{HCO}^+/\text{N}_2\text{H}^+$  (6–5) ratios, corrected for the  $\text{HCO}^+$  line opacity when available (see Table 6), that we derive toward our source sample. More specifically, the reported  $\text{HCO}^+/\text{N}_2\text{H}^+$  abundance ratios for VLA1623, NGC1333–IRAS2, Serpens–FIRS 1 and IC1396N are based on integrated line intensity ratios of the  $\text{H}^{13}\text{CO}^+$  (6–5) over  $\text{N}_2\text{H}^+$  (6–5), and assuming an isotopic  $^{12}\text{C}/^{13}\text{C}$  ratio of 68 (see Milam et al. 2005). Regarding L1641 S3 MMS 1, Cep E–mm and NGC7129–FIRS2 protostars, the measured abundance ratio is only based on the ratio between the integrated line intensity of the  $\text{HCO}^+$  (6–5) and  $\text{N}_2\text{H}^+$  (6–5) transitions. In the case of  $\tau \gg 1$ , we estimate for these 3 sources, an upper limit of the  $\text{HCO}^+/\text{N}_2\text{H}^+$  ratio (which is based on the upper limit of the  $\int T_{\text{H}^{13}\text{CO}^+(6-5)} dV$ , see Table 3) and, include it in the error bars displayed in the Figure 4.

It is noteworthy that the derived abundance ratios are given (in Fig. 4 and Table 6) sorting the source by increasing luminosities and lie in the range of  $4_{-1}^{+100}$  up to  $42_{-31}^{+31}$ .

## 5. Discussion

Numerous studies have investigated the  $\text{HCO}^+/\text{N}_2\text{H}^+$  abundance ratio toward different astrophysical environments (e.g. Turner & Thaddeus 1977; Snyder et al. 1977; Kim et al. 2006; Lo et al. 2009; Meier & Turner 2012; Sanhueza et al. 2012; Ren et al. 2014; Stephens et al. 2015, and references therein). The latter is subject to variation according to the density of the region along with its chemical content (i.e. CO) and evolutionary stage.

In particular, the  $\text{HCO}^+/\text{N}_2\text{H}^+$  ratio is expected and measured to be low in early stages of star formation ( $T < 10\text{K}$ ). This results from the adsorption of CO onto grain mantles at low temperature. In that instance,  $\text{N}_2\text{H}^+$  is unlikely to be destroyed by CO, as suggested by Eq. 4 (Bergin & Langer 1997):



On the contrary, in a more evolved stage, when CO is released in the gas-phase (typically  $T > 20\text{K}$ ), the  $\text{HCO}^+/\text{N}_2\text{H}^+$  ratio is expected to be large, since the destruction of  $\text{N}_2\text{H}^+$  by CO leads to an enhancement in  $\text{HCO}^+$  (see Eq. 4 and Bergin

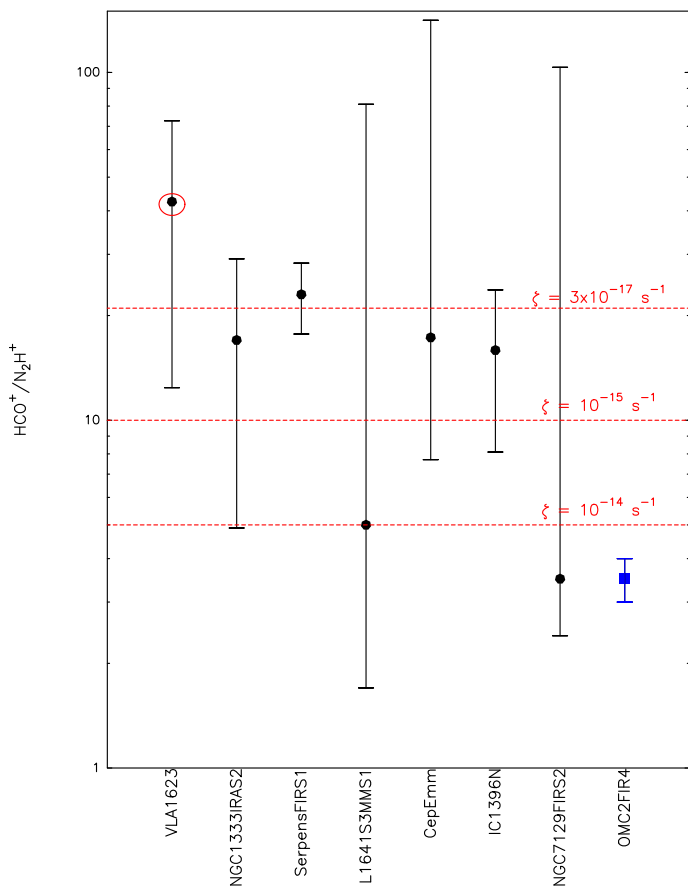


**Fig. 4.** Distribution of the  $\text{HCO}^+/\text{N}_2\text{H}^+$  abundance ratios toward our source sample (see Table 1). The sources are sorted by increasing luminosities. Full dots with error bars indicate the abundance ratios that have been corrected for the line opacity when  $\text{H}^{13}\text{CO}^+$  (6–5) observations are available (see Sections 4.1 and 4.2). Red circle marks the colder source of our sample (based on the  $\text{HCO}^+$  SLED, see Section 3.2). The blue filled square shows the  $\text{HCO}^+/\text{N}_2\text{H}^+$  ratio reported in direction of OMC-2 FIR4 by Ceccarelli et al. (2014). Finally, the red dashed lines show the predicted ratios that are expected for cosmic-rate ionization rates,  $\zeta$ , of  $10^{-14}\text{s}^{-1}$ ,  $10^{-15}\text{s}^{-1}$  and  $3\times 10^{-17}\text{s}^{-1}$ , for a gas temperature of 40 K and a  $n_{\text{H}_2}$  density of  $2.5\times 10^5\text{cm}^{-3}$  (for further details see Ceccarelli et al. 2014).

& Langer 1997). Alternatively, the  $\text{HCO}^+/\text{N}_2\text{H}^+$  ratio might be affected by the CO and  $\text{N}_2$  abundances. On the one hand, the CO abundance may be lower than the canonical value of  $10^{-4}$ : in protostellar envelopes (Alonso-Albi et al. 2010), low-mass protostars (Yıldız et al. 2010; Anderl et al. 2016) and, protoplanetary disk (e.g. Favre et al. 2013). On the other hand,  $\text{N}_2$  may not be the main Nitrogen reservoir, Nitrogen being in the atomic-form and/or in ammonia ices (e.g. Le Gal et al. 2014, and references therein). Finally, cosmic rays and X-rays might also impact this ratio (Ceccarelli et al. 2014; Bruderer et al. 2009), free electrons destroying both  $\text{HCO}^+$  and  $\text{N}_2\text{H}^+$ . Indeed, Ceccarelli et al. (2014) have shown that CR-like energetic particles (cosmic-ray ionization rate  $\zeta > 10^{-14}\text{s}^{-1}$ ) can explain the very low and unusual  $\text{HCO}^+/\text{N}_2\text{H}^+$  abundance ratio of about 3–4 that is observed toward the proto-cluster OMC-2 FIR4. Incidentally, Podio et al. (2014) have also shown that a high value of the cosmic-ray ionization rate ( $\zeta \sim 3\times 10^{-16}\text{s}^{-1}$ ) reproduces the observed  $\text{HCO}^+$  and  $\text{N}_2\text{H}^+$  abundances toward a young protostellar outflow shock. As a matter of fact, X-rays may add up with cosmic rays in the production of  $\text{H}_3^+$  and free electrons, provided

that the X-ray ionization rate is high enough, which is not the case here, as most of our source sample does not show significant X-ray emission (see Furusho et al. 2000 and the Chandra Data Archive).

Figure 5 illustrates and summarizes the main chemical  $\text{HCO}^+$  and  $\text{N}_2\text{H}^+$  destruction and formation pathways.

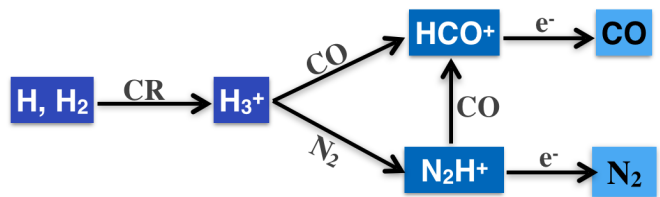


**Fig. 5.** Sketch of reactions that form and destroy  $\text{HCO}^+$  and  $\text{N}_2\text{H}^+$ : when electrons do not dominate, CO is the main destroyer of  $\text{N}_2\text{H}^+$ . However, note that there are other branching ratios which give less abundant products that are not shown in this sketch.

In that context, in Figure 4, we compare the value derived toward OMC-2 FIR4 with the ones derived from our study. In addition, we also report in Fig. 4  $\text{HCO}^+/\text{N}_2\text{H}^+$  ratios of 5, 10 and 21 that are predicted by the model of Ceccarelli et al. (2014) for a gas temperature of 40 K and a  $n_{\text{H}_2}$  density of  $2.5\times 10^5\text{cm}^{-3}$ , which are reasonable values for the gas probed by the Herschel observations presented in this work and, for a cosmic-ray ionization rate,  $\zeta$ , of  $10^{-14}\text{s}^{-1}$ ,  $10^{-15}\text{s}^{-1}$  and  $3\times 10^{-17}\text{s}^{-1}$ , respectively. Higher  $\text{HCO}^+/\text{N}_2\text{H}^+$  ratios (for example a value of 30) would correspond to lower  $\zeta$  and conversely, lower  $\text{HCO}^+/\text{N}_2\text{H}^+$  ratios would correspond to higher  $\zeta$ . We note that the case of L1641 S3 MMS 1 is interesting as the region where this source is lying contains X-ray sources (see Pillitteri et al. 2013) which may contribute to the ionization rate. Unfortunately, the error bars in our sample are relatively large and do not allow to draw firm conclusions on enhanced  $\zeta$  of X-rays in any source. On the contrary, VLA1623, Serpens FIRS1, IC1396N and CepE do not show evident signs of large  $\zeta$ . This result comes as no surprise in the case of VLA1623 and IC1396N, since their  $\text{HCO}^+$  SLEDs (see Figure 3) are strongly suggesting cold sources. Nevertheless, one notable feature of Figure 4 is that the observed  $\text{HCO}^+/\text{N}_2\text{H}^+$  ratio does not increase or decrease with increasing luminosity.

We conclude that, at the present time, OMC-2 FIR4 is the only source where a high flux of energetic particles is clearly evident. Unfortunately, the statistics are small, so that we cannot infer what makes OMC-2 FIR4 special in that respect. More sensitive observations, especially toward NGC7129–FIRS2 and L1641 S3 MMS 1 (see pattern of the  $\text{HCO}^+$  SLED along with the obtained  $\text{HCO}^+/\text{N}_2\text{H}^+$  ratio in Figures 3 and 4), and in a much larger sample are necessary to say more.

## 6. Conclusions

We have investigated the  $\text{HCO}^+/\text{N}_2\text{H}^+$  abundance ratio toward a sample of low- and intermediate-mass protostars, through observations performed with the HIFI instrument on board the Herschel Space Observatory. Our study is based on the analysis of high  $J$  transitions ( $6 \leq J \leq 12$ ) of the  $\text{HCO}^+$ ,  $\text{N}_2\text{H}^+$  and  $\text{H}^{13}\text{CO}^+$  ions.

All the targeted  $\text{HCO}^+$  transitions have been detected in the majority of the sources. More specifically, the lowest lying transition (6–5) is detected toward all the 9 surveyed sources for  $\text{HCO}^+$  and, in 7 of them for  $\text{N}_2\text{H}^+$ . Regarding  $\text{H}^{13}\text{CO}^+$ , the (6–5)



line is only detected toward four out of the nine sources. Assuming a  $^{12}\text{C}/^{13}\text{C}$  isotopic ratio of 68, we report a  $\text{HCO}^+/\text{N}_2\text{H}^+$  abundance ratio in the range of  $4_{-1}^{+100}$  up to  $42_{-31}^{+31}$ . The latter might even be lower depending on the opacity of the  $\text{N}_2\text{H}^+$  (6–5) transition. Incidentally, a salient result is that the measured  $\text{HCO}^+/\text{N}_2\text{H}^+$  ratio does not increase or decrease with increasing luminosity, which suggests that UV radiation does not play a major role in the  $\text{HCO}^+/\text{N}_2\text{H}^+$  abundance ratio. However, our measurements have large error bars that prevent us from determining whether OMC-2 FIR4 is the only source where a high flux of energetic particles is observed. Therefore, further sensitive and high angular resolution observations toward a much larger source sample are necessary *i)* to ascertain whether OMC-2 FIR4 is a peculiar source and, *ii)* to accurately infer the flux of energetic particles at the interior of the protostar envelopes if applicable.

**Acknowledgements.** Support for this work was provided by the French space agency CNES. MP acknowledges funding from the European Unions Horizon 2020 research and innovation programme under the Marie Skłodowska-Curie grant agreement No 664931. Support for this work was also provided by NASA (Herschel OT funding) through an award issued by JPL/Caltech. This paper makes use of Herschel/HIFI data. Herschel is an ESA space observatory with science instruments provided by European-led principal Investigator consortia and with important participation from NASA. HIFI has been designed and built by a consortium of institutes and university departments from across Europe, Canada, and the United States under the leadership of SRON Netherlands Institute for Space Research, Groningen, The Netherlands and with major contributions from Germany, France, and the U.S. Consortium members are: Canada: CSA, U. Waterloo; France: CESR, LAB, LERMA, IRAM; Germany: KOSMA, MPIfR, MPS; Ireland: NUI Maynooth; Italy: ASI, IFSI-INAF, Osservatorio Astrofisico di Arcetri-INAF; Netherlands: SRON, TUD; Poland: CAMK, CBK; Spain: Observatorio Astronómico Nacional (IGN), Centro de Astrobiología (CSIC-INTA); Sweden: Chalmers University of Technology–MC2, RSS and GARD, Onsala Space Observatory, Swedish National Space Board, Stockholm Observatory; Switzerland: ETH Zurich, FHNW; USA: Caltech, JPL, NHSC.

## References

- Alonso-Albi, T., Fuente, A., Crimier, N., et al. 2010, *A&A*, 518, A52  
Amano, T., Hirao, T., & Takano, J. 2005, *Journal of Molecular Spectroscopy*, 234, 170  
Anderl, S., Maret, S., Cabrit, S., et al. 2016, *A&A*, 591, A3  
Andre, P., Ward-Thompson, D., & Barsony, M. 1993, *ApJ*, 406, 122  
Bergin, E. A. & Langer, W. D. 1997, *ApJ*, 486, 316  
Botschwina, P., Horn, M., Flugge, J., & Seeger, S. 1993, *J. Chem. Soc.*, 89, 2219  
Bricker, G. E. & Caffee, M. W. 2010, *ApJ*, 725, 443  
Bruderer, S., Doty, S. D., & Benz, A. O. 2009, *ApJS*, 183, 179  
Caselli, P., Myers, P. C., & Thaddeus, P. 1995, *ApJ*, 455, L77  
Ceccarelli, C., Bacmann, A., Boogert, A., et al. 2010, *A&A*, 521, L22  
Ceccarelli, C., Dominik, C., López-Sepulcre, A., et al. 2014, *ApJ*, 790, L1  
Ceccarelli, C., Hily-Blant, P., Montmerle, T., et al. 2011, *ApJ*, 740, L4  
Cernis, K. 1990, *Ap&SS*, 166, 315  
Crimier, N., Ceccarelli, C., Alonso-Albi, T., et al. 2010, *A&A*, 516, A102  
Davies, P. B. & Rothwell, W. J. 1984, *J. Chem. Phys.*, 81, 5239  
de Graauw, T., Helmich, F. P., Phillips, T. G., et al. 2010, *A&A*, 518, L6  
Desch, S. J., Connolly, Jr., H. C., & Srinivasan, G. 2004, *ApJ*, 602, 528  
Favre, C., Cleaves, L. I., Bergin, E. A., Qi, C., & Blake, G. A. 2013, *ApJ*, 776, L38  
Giannini, T., Nisini, B., & Lorenzetti, D. 2001, *ApJ*, 555, 40  
Goldsmith, P. F. & Langer, W. D. 1999, *ApJ*, 517, 209  
Gounelle, M., Chaussidon, M., & Rollion-Bard, C. 2013, *ApJ*, 763, L33  
Gounelle, M., Shu, F. H., Shang, H., et al. 2006, *ApJ*, 640, 1163  
Gregersen, E. M. & Evans, II, N. J. 2001, *ApJ*, 553, 1042  
Havenith, M., Zwart, E., Leo Meerts, W., & Ter Meulen, J. J. 1990, *J. Chem. Phys.*, 93, 8446  
Hayakawa, S. 1952, *Progress of Theoretical Physics*, 8, 571  
Hirota, E. & Endo, Y. 1988, *Journal of Molecular Spectroscopy*, 127, 527  
Hoq, S., Jackson, J. M., Foster, J. B., et al. 2013, *ApJ*, 777, 157  
Indriolo, N., Blake, G. A., Goto, M., et al. 2010, *ApJ*, 724, 1357  
Jørgensen, J. K., Bourke, T. L., Myers, P. C., et al. 2007, *ApJ*, 659, 479  
Jørgensen, J. K., Hogerheijde, M. R., van Dishoeck, E. F., Blake, G. A., & Schöier, F. L. 2004, *A&A*, 413, 993  
Karska, A., Herczeg, G. J., van Dishoeck, E. F., et al. 2013, *A&A*, 552, A141  
Kawaguchi, K., Yamada, C., Saito, S., & Hirota, E. 1985, *J. Chem. Phys.*, 82, 1750  
Kim, S.-J., Kim, H.-D., Lee, Y., et al. 2006, *ApJS*, 162, 161  
Kristensen, L. E., van Dishoeck, E. F., Bergin, E. A., et al. 2012, *A&A*, 542, A8  
Lattanzi, V., Walters, A., Drouin, B. J., & Pearson, J. C. 2007, *ApJ*, 662, 771  
Le Gal, R., Hily-Blant, P., Faure, A., et al. 2014, *A&A*, 562, A83  
Lo, N., Cunningham, M. R., Jones, P. A., et al. 2009, *MNRAS*, 395, 1021  
Loinard, L., Torres, R. M., Mioduszewski, A. J., & Rodríguez, L. F. 2008, *ApJ*, 675, L29  
López-Sepulcre, A., Jaber, A. A., Mendoza, E., et al. 2015, *MNRAS*, 449, 2438  
López-Sepulcre, A., Taquet, V., Sánchez-Monge, Á., et al. 2013, *A&A*, 556, A62  
Maury, A., Ohashi, N., & André, P. 2012, *A&A*, 539, A130  
Meier, D. S. & Turner, J. L. 2012, *ApJ*, 755, 104  
Milam, S. N., Savage, C., Brewster, M. A., Ziurys, L. M., & Wyckoff, S. 2005, *ApJ*, 634, 1126  
Müller, H. S. P., Schlöder, F., Stutzki, J., & Winnewisser, G. 2005, *Journal of Molecular Structure*, 742, 215  
Padovani, M., Hennebelle, P., Marcowith, A., & Ferrière, K. 2015, *A&A*, 582, L13  
Padovani, M., Marcowith, A., Hennebelle, P., & Ferrière, K. 2016, *A&A*, 590, A8  
Pagani, L., Daniel, F., & Dubernet, M.-L. 2009, *A&A*, 494, 719  
Pilbratt, G. L., Riedinger, J. R., Passvogel, T., et al. 2010, *A&A*, 518, L1  
Podio, L., Lefloch, B., Ceccarelli, C., Codella, C., & Bachiller, R. 2014, *A&A*, 565, A64  
Remijan, A. J., Markwick-Kemper, A., & ALMA Working Group on Spectral Line Frequencies. 2007, *BAAS*, 38, 963  
Ren, Z., Li, D., & Chapman, N. 2014, *ApJ*, 788, 172  
Roelfsema, P. R., Helmich, F. P., Teysseier, D., et al. 2012, *A&A*, 537, A17  
Sanhueza, P., Jackson, J. M., Foster, J. B., et al. 2012, *ApJ*, 756, 60  
Schmid-Burgk, J., Muters, D., Müller, H. S. P., & Brupbacher-Gatehouse, B. 2004, *A&A*, 419, 949  
Shimajiri, Y., Takahashi, S., Takakuwa, S., Saito, M., & Kawabe, R. 2008, *ApJ*, 683, 255  
Snyder, L. E., Hollis, J. M., & Watson, W. D. 1977, *ApJ*, 212, 79  
Stäuber, P., Doty, S. D., van Dishoeck, E. F., & Benz, A. O. 2005, *A&A*, 440, 949  
Stäuber, P., Jørgensen, J. K., van Dishoeck, E. F., Doty, S. D., & Benz, A. O. 2006, *A&A*, 453, 555  
Stecker, F. W., Vette, J. I., & Trombka, J. I. 1971, *Nature Physical Science*, 231, 122  
Stephens, I. W., Jackson, J. M., Sanhueza, P., et al. 2015, *ApJ*, 802, 6  
Straizys, V., Cernis, K., Kazlauskas, A., & Meistas, E. 1992, *Baltic Astronomy*, 1, 149  
Tinti, F., Bizzocchi, L., Degli Esposti, C., & Dore, L. 2007, *ApJ*, 669, L113  
Turner, B. E. & Thaddeus, P. 1977, *ApJ*, 211, 755  
Verhooe, P., Zwart, E., Versluis, M., et al. 1990, *Review of Scientific Instruments*, 61, 1612  
Yıldız, U. A., van Dishoeck, E. F., Kristensen, L. E., et al. 2010, *A&A*, 521, L40

### **Appendix A: HCO<sup>+</sup>, H<sup>13</sup>CO<sup>+</sup> and N<sub>2</sub>H<sup>+</sup> toward our sample of intermediate and low-mass protostars**

Figures A.1 to A.7 display the respective spectra of the HCO<sup>+</sup>, H<sup>13</sup>CO<sup>+</sup> and N<sub>2</sub>H<sup>+</sup> transitions observed with Herschel toward a portion of our source sample (see Section 3). Note that for display purposes, the spectra have been smoothed at a spectral resolution of 4.4 MHz.

### **Appendix B: Transitions of HCO<sup>+</sup>, H<sup>13</sup>CO<sup>+</sup> and N<sub>2</sub>H<sup>+</sup> observed with Herschel toward our sample of intermediate and low-mass protostars**

Tables B.1 to B.9 summarize the line parameters for all the HCO<sup>+</sup>, H<sup>13</sup>CO<sup>+</sup> and N<sub>2</sub>H<sup>+</sup> transitions observed with Herschel toward our source sample (see Section 3).

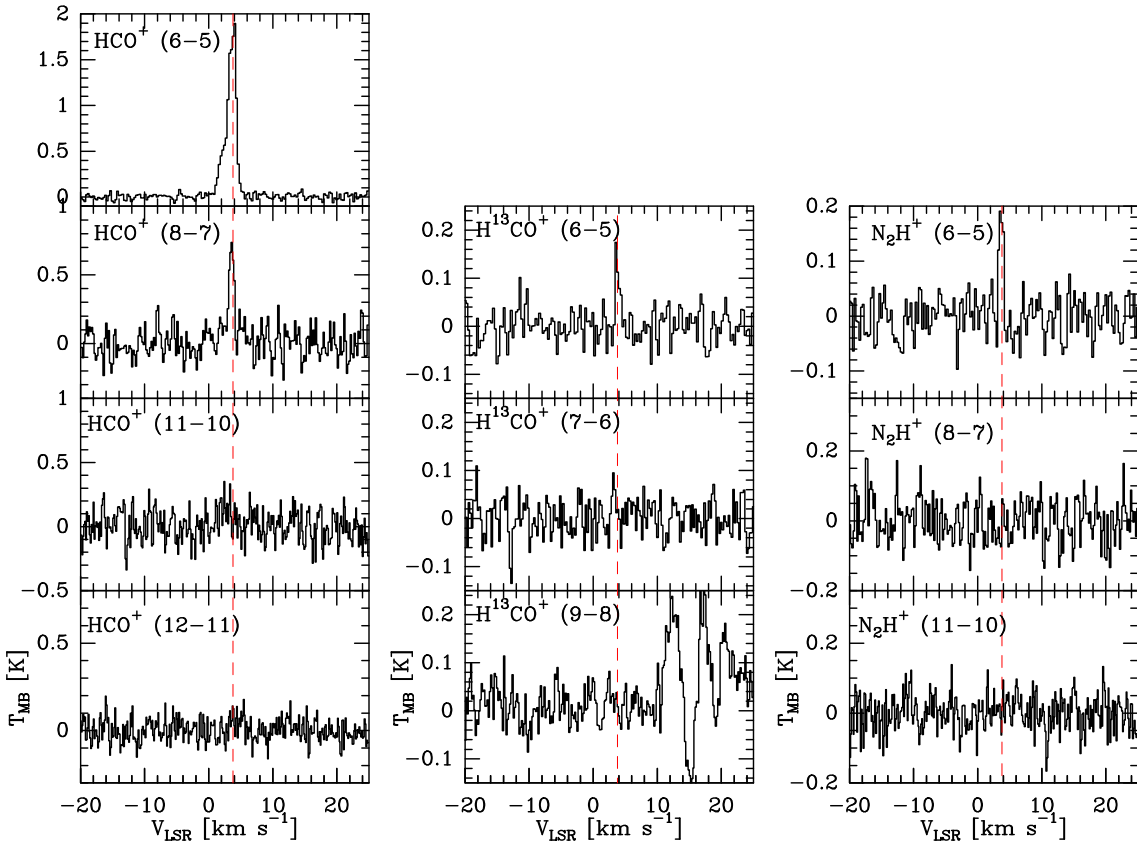


**Fig. A.1.** Spectra observed toward VLA1623. Dashed red lines indicate a  $v_{LSR} = 3.8 \text{ km s}^{-1}$ . The observed transition is indicated on each plot.

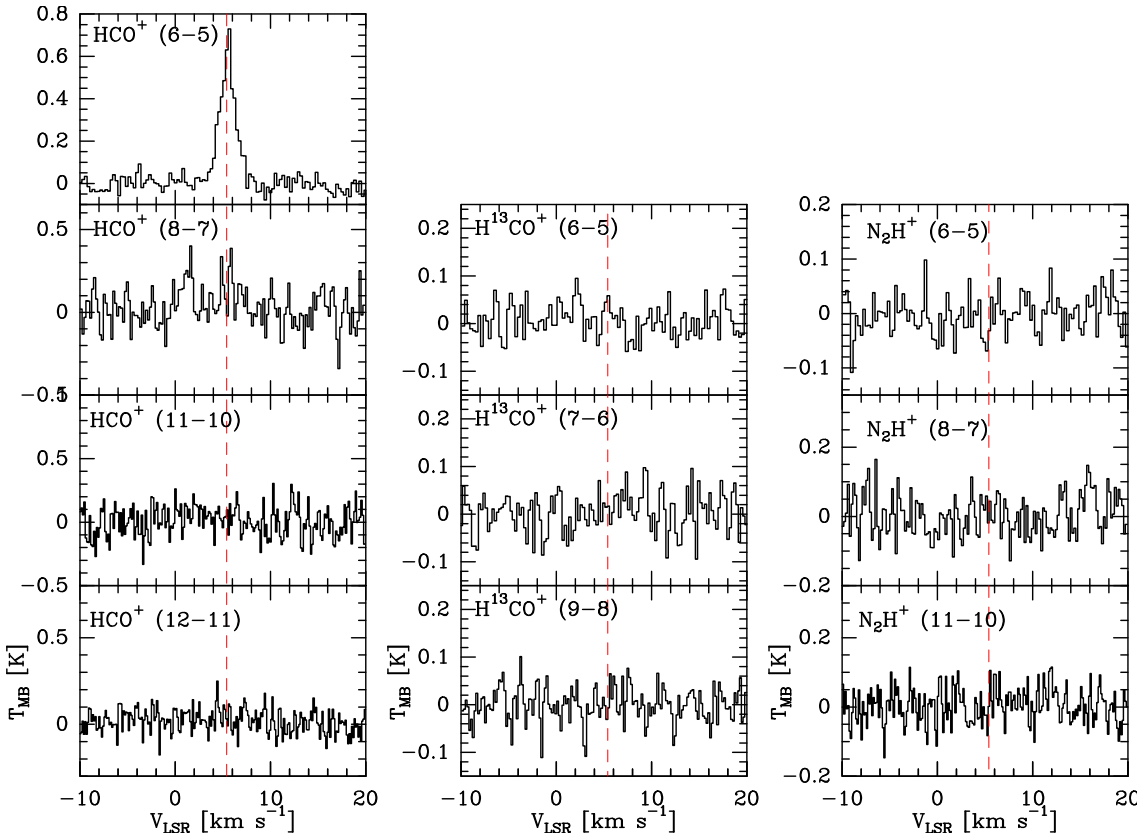


**Fig. A.2.** Spectra observed toward L1527. Dashed red lines indicate a  $v_{LSR} = 5.4 \text{ km s}^{-1}$ . The observed transition is indicated on each plot.

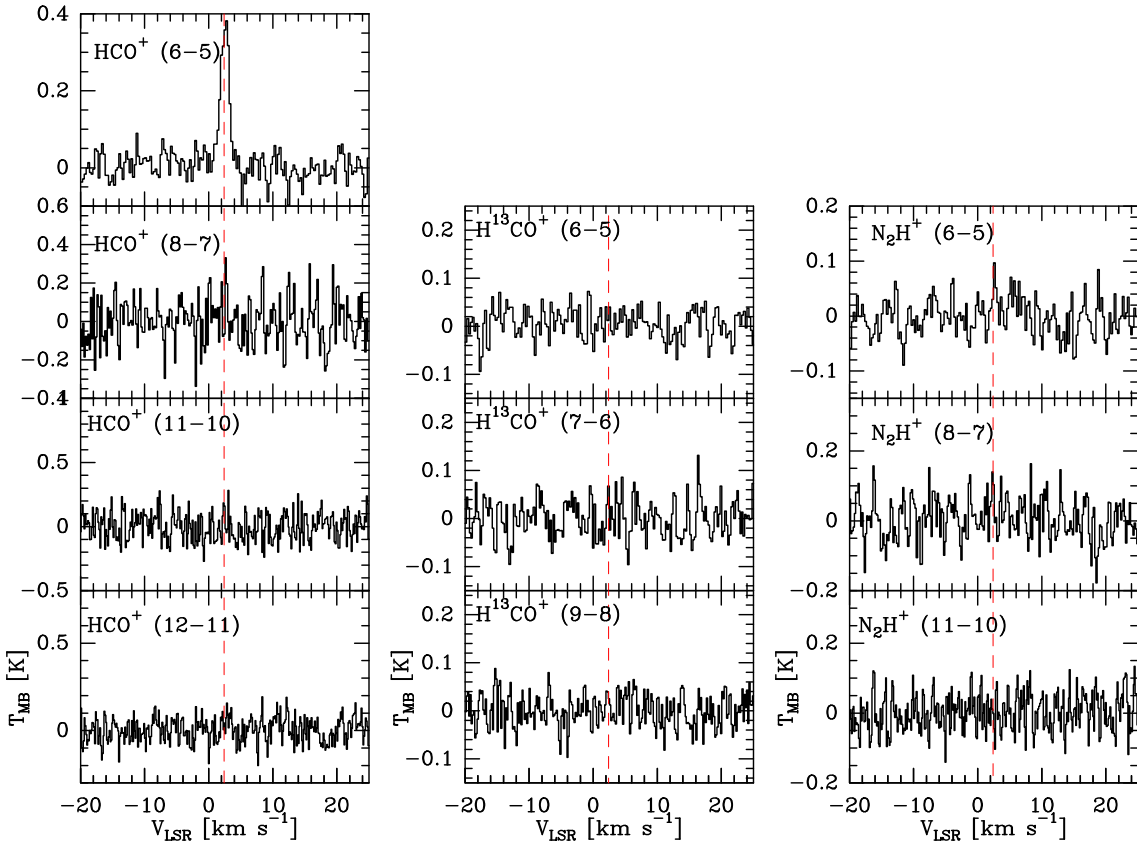


**Fig. A.3.** Spectra observed toward L1157-MM. Dashed red lines indicate a  $v_{LSR} = 2.4 \text{ km s}^{-1}$ . The observed transition is indicated on each plot.

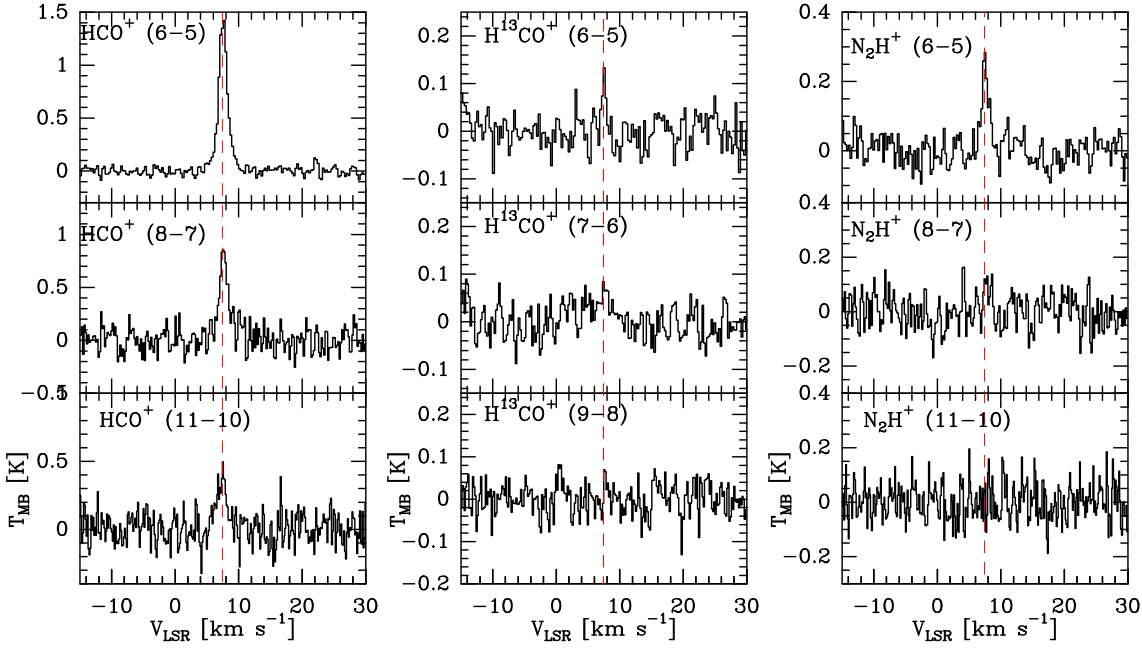


**Fig. A.4.** Spectra observed toward NGC1333-IRAS2. Dashed red lines indicate a  $v_{LSR} = 7.45 \text{ km s}^{-1}$ . The observed transition is indicated on each plot.

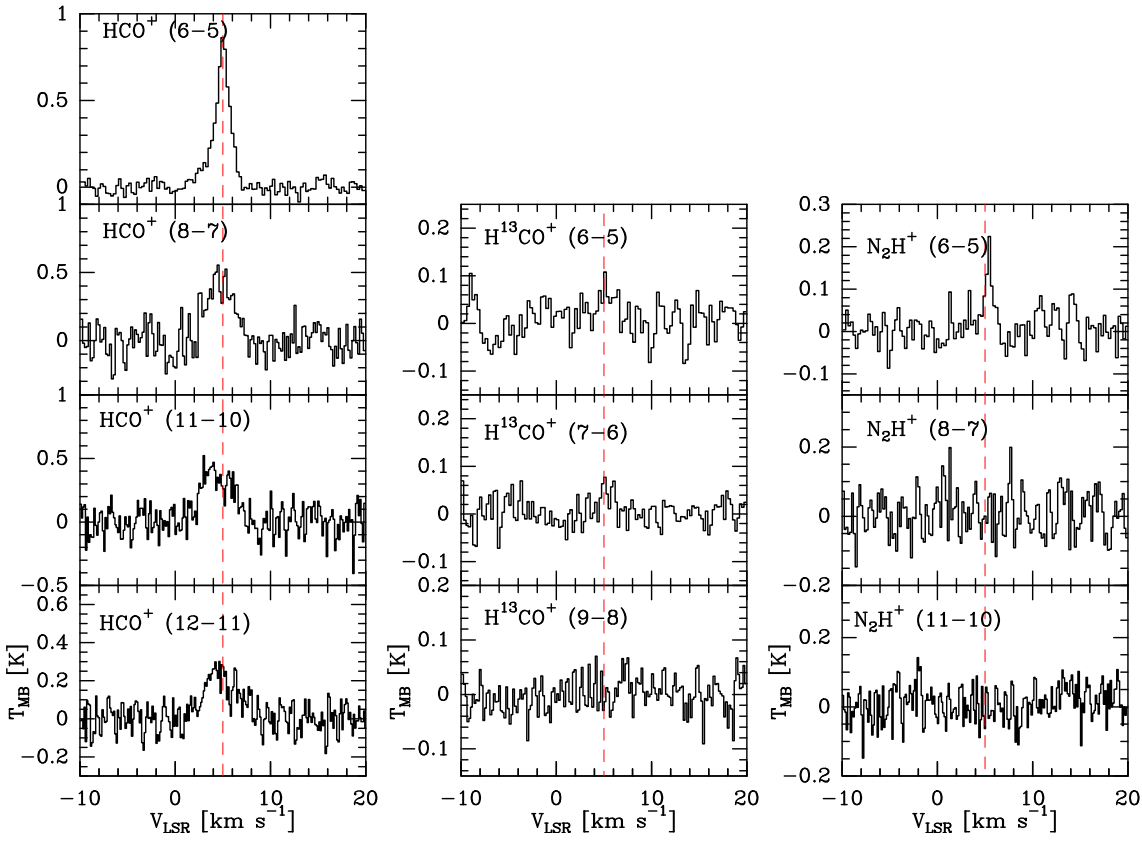


**Fig. A.5.** Spectra observed toward L1641 S3 MMS 1. Dashed red lines indicate a  $v_{LSR} = 5.0 \text{ km s}^{-1}$ . The observed transition is indicated on each plot.

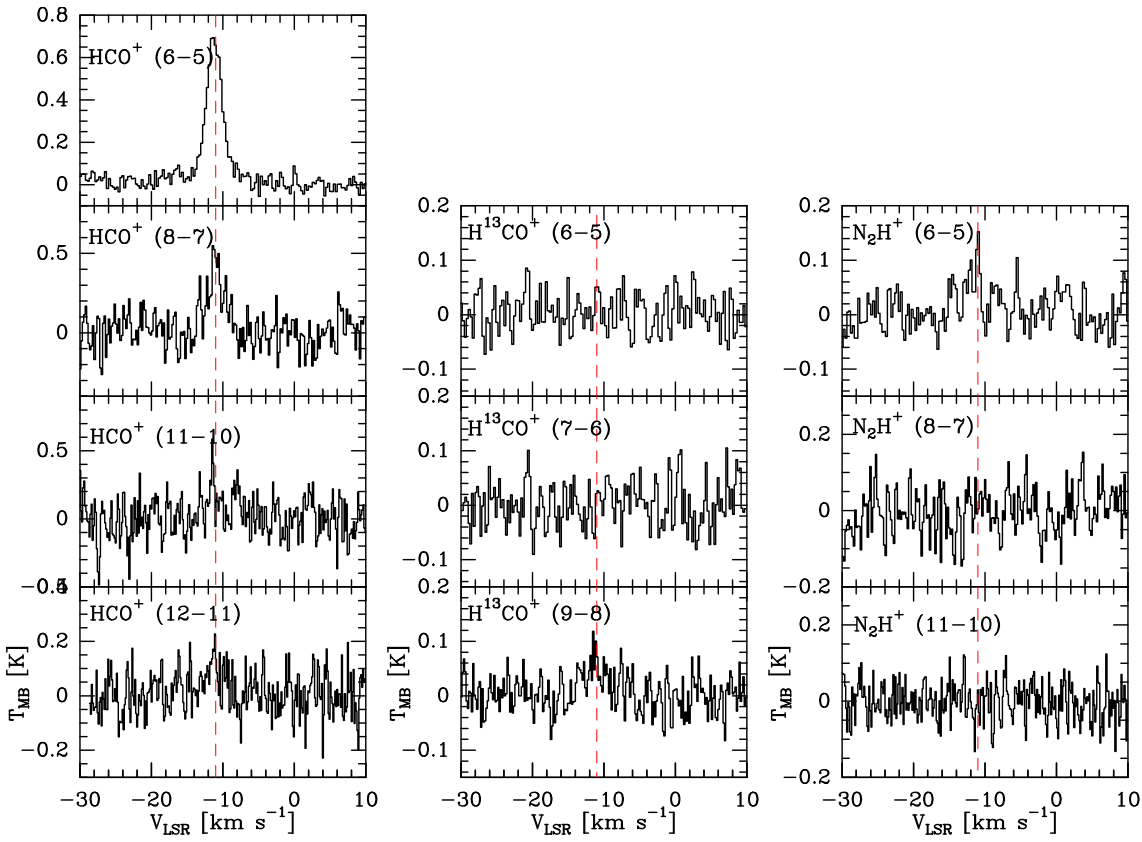


**Fig. A.6.** Spectra observed toward Cep E-mm. Dashed red lines indicate a  $v_{LSR} = -11.0 \text{ km s}^{-1}$ . The observed transition is indicated on each plot.

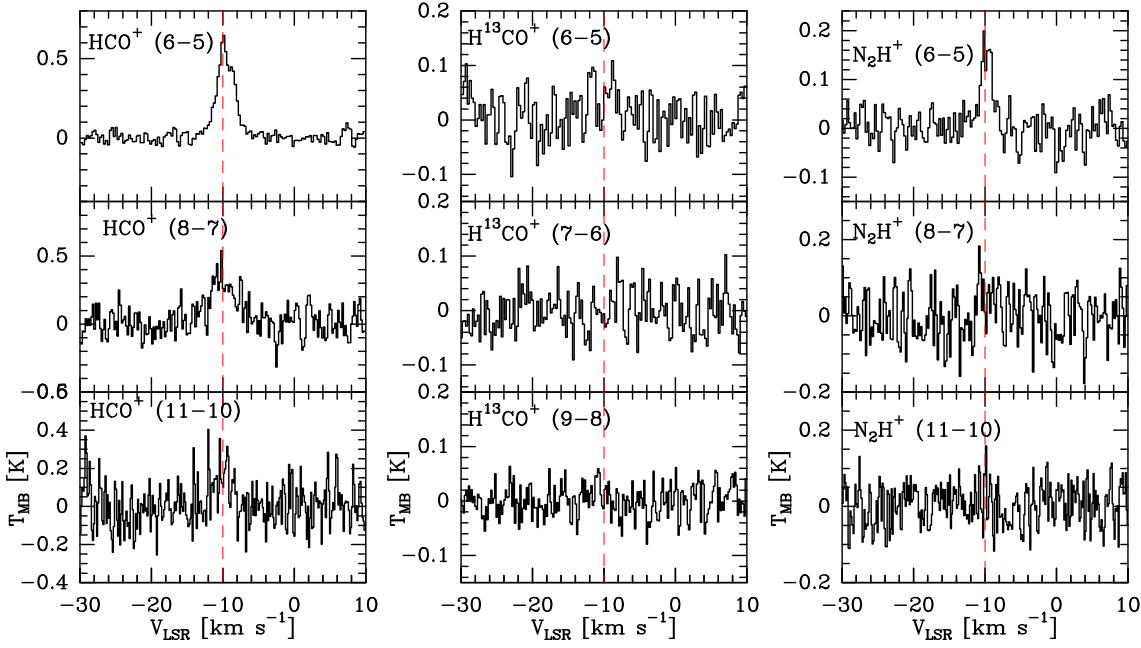


**Fig. A.7.** Spectra observed toward NGC7129–FIRS2. Dashed red lines indicate a  $v_{LSR} = -9.7$  km s $^{-1}$ . The observed transition is indicated on each plot.

**Table B.1.** Line Parameters for the HCO $^{+}$ , H $^{13}$ CO $^{+}$  and N $_2$ H $^{+}$  transitions observed toward Serpens–FIRS 1.

Frequency (MHz) (1)	$E_{up}$ (K) (2)	$S\mu^2$ (D $^2$ ) (3)	$v$ (km s $^{-1}$ ) (4)	$\Delta v_{1/2}$ (km s $^{-1}$ ) (5)	$T_{MB}$ (K) (6)	$\int T_{MB}dV$ (K km s $^{-1}$ ) (7)	Comments (8)
HCO $^{+}$							
535061.581	89.9	90.7	8.2(0.1)	2.7(0.2)	1.3(0.1)	3.8(0.6)	D
713341.228	154.1	120.9	8.1(0.2)	3.1(0.4)	0.9(0.1)	3.2(0.3)	D
980636.494	282.4	166.2	7.6(0.2)	3.2(0.5)	0.6(0.4)	1.9(0.3)	D
1069693.891	333.8	181.3	–	–	–	–	NO
H $^{13}$ CO $^{+}$							
520459.884	87.4	90.7	8.3(0.2)	1.7(0.5)	0.2(0.1)	0.41(0.09)	D
607174.646	116.6	105.8	8.3(0.2)	1.6(0.7)	0.2(0.1)	0.29(0.09)	D
780562.812	187.3	136.1	8.2(0.3)	0.8(0.5)	0.09(0.09)	0.08(0.06)	TD
N $_2$ H $^{+}$							
558966.503	93.9	669.5	8.42(0.06)	1.7(0.1)	0.7(0.1)	1.21(0.09)	D
745209.868	161.0	891.6	8.2(0.2)	2.1(0.4)	0.3(0.2)	0.7(0.1)	D
1024443.025	295.1	1223.1	8.3(0.3)	0.7(0.5)	0.1(0.1)	0.10(0.08)	TD

**Notes.** (1)–(3) Spectroscopic line parameters (see references listed in Table 2) of the observed transitions. (4)–(7) Observed line parameters: velocity, linewidth, peak temperature and integrated intensities. The  $3\sigma$  uncertainties that result from gaussian fits performed with the CLASS software are given in brackets. (8) D: Detected above the  $3\sigma$  level and  $\int T_{MB}dV \geq 5\sigma$ , TD: Tentative Detection (line that emits at the  $3\sigma$ ), NO: Not observed.

**Table B.2.** Line Parameters for the HCO<sup>+</sup>, H<sup>13</sup>CO<sup>+</sup> and N<sub>2</sub>H<sup>+</sup> transitions observed toward IC1396N.

Frequency (MHz) (1)	E <sub>up</sub> (K) (2)	Sμ <sup>2</sup> (D <sup>2</sup> ) (3)	v (km s <sup>-1</sup> ) (4)	Δv <sub>1/2</sub> (km s <sup>-1</sup> ) (5)	T <sub>MB</sub> (K) (6)	∫T <sub>MB</sub> dV (K km s <sup>-1</sup> ) (7)	Comments (8)
HCO <sup>+</sup>							
535061.581	89.9	90.7	0.27(0.03)	2.8(0.1)	2.3(0.1)	6.7(0.6)	D
713341.228	154.1	120.9	0.7(0.2)	2.8(0.6)	1.1(0.2)	3.4(0.5)	D
980636.494	282.4	166.2	0.7(0.2)	4.0(0.2)	0.5(0.4)	2.24(0.05)	D
1069693.891	333.8	181.3	0.7(0.2)	3.8(0.2)	0.3(0.2)	1.31(0.03)	D
H <sup>13</sup> CO <sup>+</sup>							
520459.884	87.4	90.7	0.4(0.6)	2.02(1.55)	0.09(0.10)	0.21(0.10)	W
607174.646	116.6	105.8	0.5(0.9)	2.4(1.7)	0.08(0.08)	0.2(0.1)	TD
780562.812	187.3	136.1	–	–	≤0.1	≤0.4	ND
N <sub>2</sub> H <sup>+</sup>							
558966.503	93.9	669.5	0.2(0.1)	2.4(0.4)	0.4(0.1)	0.9(0.1)	D
745209.868	161.0	891.6	0.01(0.49)	3.4(1.1)	0.2(0.2)	0.8(0.2)	W
1024443.025	295.1	1223.1	–	–	≤0.2	≤0.6	ND

**Notes.** (1)–(3) Spectroscopic line parameters (see references listed in Table 2) of the observed transitions. (4)–(7) Observed line parameters: velocity, linewidth, peak temperature and integrated intensities. The 3σ uncertainties that result from gaussian fits performed with the CLASS software are given in brackets. (8) D: Detected above the 3σ level and ∫T<sub>MB</sub>dV ≥ 5σ, W: Weak line (∫T<sub>MB</sub>dV ≥ 5σ), ND: Not Detected lines (T<sub>MB</sub> < 3σ and ∫T<sub>MB</sub>dV < 5σ), TD: Tentative Detection (line that emits at the 3σ).

**Table B.3.** Line Parameters for the HCO<sup>+</sup>, H<sup>13</sup>CO<sup>+</sup> and N<sub>2</sub>H<sup>+</sup> transitions observed toward VLA1623.

Frequency (MHz) (1)	E <sub>up</sub> (K) (2)	Sμ <sup>2</sup> (D <sup>2</sup> ) (3)	v (km s <sup>-1</sup> ) (4)	Δv <sub>1/2</sub> (km s <sup>-1</sup> ) (5)	T <sub>MB</sub> (K) (6)	∫T <sub>MB</sub> dV (K km s <sup>-1</sup> ) (7)	Comments (8)
HCO <sup>+</sup>							
535061.581	89.9	90.7	3.82(0.04)	1.2(0.1)	1.7(0.1)	2.2(0.4)	D
713341.228	154.1	120.9	3.6(0.1)	0.9(0.3)	0.8(0.4)	0.7(0.2)	D
980636.494	282.4	166.2	–	–	≤0.5	≤0.5	ND
1069693.891	333.8	181.3	–	–	≤0.3	≤0.3	ND
H <sup>13</sup> CO <sup>+</sup>							
520459.884	87.4	90.7	3.7(0.2)	0.5(0.5)	0.2(0.1)	0.10(0.06)	D
607174.646	116.6	105.8	–	–	≤0.2	≤0.2	ND
780562.812	187.3	136.1	–	–	≤0.3	≤0.3	ND
N <sub>2</sub> H <sup>+</sup>							
558966.503	93.9	669.5	3.7(0.1)	0.7(0.2)	0.2(0.1)	0.16(0.06)	D
745209.868	161.0	891.6	–	–	≤0.3	≤0.3	ND
1024443.025	295.1	1223.1	–	–	≤0.2	≤0.2	ND

**Notes.** (1)–(3) Spectroscopic line parameters (see references listed in Table 2) of the observed transitions. (4)–(7) Observed line parameters: velocity, linewidth, peak temperature and integrated intensities. The 3σ uncertainties that result from gaussian fits performed with the CLASS software are given in brackets. (8) D: Detected above the 3σ level and ∫T<sub>MB</sub>dV ≥ 5σ, ND: Not Detected lines (T<sub>MB</sub> < 3σ and ∫T<sub>MB</sub>dV < 5σ).

**Table B.4.** Line Parameters for the HCO<sup>+</sup>, H<sup>13</sup>CO<sup>+</sup> and N<sub>2</sub>H<sup>+</sup> transitions observed toward L1527.

Frequency (MHz) (1)	E <sub>up</sub> (K) (2)	Sμ <sup>2</sup> (D <sup>2</sup> ) (3)	v (km s <sup>-1</sup> ) (4)	Δv <sub>1/2</sub> (km s <sup>-1</sup> ) (5)	T <sub>MB</sub> (K) (6)	∫T <sub>MB</sub> dV (K km s <sup>-1</sup> ) (7)	Comments (8)
HCO <sup>+</sup>							
535061.581	89.9	90.7	5.52(0.07)	1.9(0.2)	0.6(0.1)	1.26(0.09)	D
713341.228	154.1	120.9	–	–	≤0.4	≤0.8	ND
980636.494	282.4	166.2	–	–	≤0.5	≤1.0	ND
1069693.891	333.8	181.3	–	–	≤0.3	≤0.6	ND
H <sup>13</sup> CO <sup>+</sup>							
520459.884	87.4	90.7	–	–	≤0.2	≤0.3	ND
607174.646	116.6	105.8	–	–	≤0.2	≤0.4	ND
780562.812	187.3	136.1	–	–	≤0.2	≤0.3	ND
N <sub>2</sub> H <sup>+</sup>							
558966.503	93.9	669.5	–	–	≤0.2	≤0.3	ND
745209.868	161.0	891.6	–	–	≤0.3	≤0.5	ND
1024443.025	295.1	1223.1	–	–	≤0.2	≤0.4	ND

**Notes.** (1)–(3) Spectroscopic line parameters (see references listed in Table 2) of the observed transitions. (4)–(7) Observed line parameters: velocity, linewidth, peak temperature and integrated intensities. The 3σ uncertainties that result from gaussian fits performed with the CLASS software are given in brackets. (8) D: Detected above the 3σ level and ∫T<sub>MB</sub>dV ≥ 5σ, ND: Not Detected lines (T<sub>MB</sub> < 3σ and ∫T<sub>MB</sub>dV < 5σ).

**Table B.5.** Line Parameters for the HCO<sup>+</sup>, H<sup>13</sup>CO<sup>+</sup> and N<sub>2</sub>H<sup>+</sup> transitions observed toward L1157–MM.

Frequency (MHz) (1)	E <sub>up</sub> (K) (2)	Sμ <sup>2</sup> (D <sup>2</sup> ) (3)	v (km s <sup>-1</sup> ) (4)	Δv <sub>1/2</sub> (km s <sup>-1</sup> ) (5)	T <sub>MB</sub> (K) (6)	∫T <sub>MB</sub> dV (K km s <sup>-1</sup> ) (7)	Comments (8)
HCO <sup>+</sup>							
535061.581	89.9	90.7	2.5(0.1)	1.5(0.2)	0.4(0.1)	0.63(0.09)	D
713341.228	154.1	120.9	–	–	≤0.5	≤0.8	ND
980636.494	282.4	166.2	–	–	≤0.5	≤0.8	ND
1069693.891	333.8	181.3	–	–	≤0.3	≤0.5	ND
H <sup>13</sup> CO <sup>+</sup>							
520459.884	87.4	90.7	–	–	≤0.1	≤0.2	ND
607174.646	116.6	105.8	–	–	≤0.2	≤0.3	ND
780562.812	187.3	136.1	–	–	≤0.1	≤0.2	ND
N <sub>2</sub> H <sup>+</sup>							
558966.503	93.9	669.5	–	–	≤0.1	≤0.2	ND
745209.868	161.0	891.6	–	–	≤0.3	≤0.4	ND
1024443.025	295.1	1223.1	–	–	≤0.2	≤0.3	ND

**Notes.** (1)–(3) Spectroscopic line parameters (see references listed in Table 2) of the observed transitions. (4)–(7) Observed line parameters: velocity, linewidth, peak temperature and integrated intensities. The 3σ uncertainties that result from gaussian fits performed with the CLASS software are given in brackets. (8) D: Detected above the 3σ level and ∫T<sub>MB</sub>dV ≥ 5σ, ND: Not Detected lines (T<sub>MB</sub> < 3σ and ∫T<sub>MB</sub>dV < 5σ).



**Table B.6.** Line Parameters for the HCO<sup>+</sup>, H<sup>13</sup>CO<sup>+</sup> and N<sub>2</sub>H<sup>+</sup> transitions observed toward NGC1333–IRAS2.

Frequency (MHz) (1)	E <sub>up</sub> (K) (2)	Sμ <sup>2</sup> (D <sup>2</sup> ) (3)	v (km s <sup>-1</sup> ) (4)	Δv <sub>1/2</sub> (km s <sup>-1</sup> ) (5)	T <sub>MB</sub> (K) (6)	∫T <sub>MB</sub> dV (K km s <sup>-1</sup> ) (7)	Comments (8)
HCO <sup>+</sup>							
535061.581	89.9	90.7	7.52(0.04)	1.2(0.2)	1.03(0.09)	1.4(0.6)	D
713341.228	154.1	120.9	7.6(0.2)	1.7(0.5)	0.8(0.5)	1.5(0.3)	D
980636.494	282.4	166.2	7.3(0.3)	1.9(0.8)	0.4(0.3)	0.8(0.3)	D
1069693.891	333.8	181.3	–	–	–	–	NO
H <sup>13</sup> CO <sup>+</sup>							
520459.884	87.4	90.7	7.5(0.2)	0.7(0.4)	0.1(0.1)	0.09(0.06)	W
607174.646	116.6	105.8	–	–	≤0.1	≤0.1	ND
780562.812	187.3	136.1	–	–	≤0.1	≤0.1	ND
N <sub>2</sub> H <sup>+</sup>							
558966.503	93.9	669.5	7.6(0.2)	1.3(0.4)	0.3(0.2)	0.36(0.09)	D
745209.868	161.0	891.6	–	–	≤0.3	≤0.6	ND
1024443.025	295.1	1223.1	–	–	≤0.3	≤0.6	ND

**Notes.** (1)–(3) Spectroscopic line parameters (see references listed in Table 2) of the observed transitions. (4)–(7) Observed line parameters: velocity, linewidth, peak temperature and integrated intensities. The 3σ uncertainties that result from gaussian fits performed with the CLASS software are given in brackets. (8) D: Detected above the 3σ level and ∫T<sub>MB</sub>dV ≥ 5σ, W: Weak line (∫T<sub>MB</sub>dV ≥ 5σ), ND: Not Detected lines (T<sub>MB</sub> < 3σ and ∫T<sub>MB</sub>dV < 5σ), NO: Not observed.

**Table B.7.** Line Parameters for the HCO<sup>+</sup>, H<sup>13</sup>CO<sup>+</sup> and N<sub>2</sub>H<sup>+</sup> transitions observed toward L1641 S3 MMS 1.

Frequency (MHz) (1)	E <sub>up</sub> (K) (2)	Sμ <sup>2</sup> (D <sup>2</sup> ) (3)	v (km s <sup>-1</sup> ) (4)	Δv <sub>1/2</sub> (km s <sup>-1</sup> ) (5)	T <sub>MB</sub> (K) (6)	∫T <sub>MB</sub> dV (K km s <sup>-1</sup> ) (7)	Comments (8)
HCO <sup>+</sup>							
535061.581	89.9	90.7	5.09(0.07)	1.4(0.3)	0.6(0.1)	0.9(0.4)	D
713341.228	154.1	120.9	4.7(0.4)	3.1(0.7)	0.5(0.5)	1.5(0.3)	W
980636.494	282.4	166.2	4.3(0.4)	3.7(0.7)	0.4(0.5)	1.6(0.3)	W
1069693.891	333.8	181.3	4.7(0.3)	4.0(0.8)	0.2(0.3)	1.0(0.3)	W
H <sup>13</sup> CO <sup>+</sup>							
520459.884	87.4	90.7	–	–	≤0.2	≤0.2	ND
607174.646	116.6	105.8	–	–	≤0.1	≤0.1	ND
780562.812	187.3	136.1	–	–	≤0.1	≤0.1	ND
N <sub>2</sub> H <sup>+</sup>							
558966.503	93.9	669.5	5.4(0.2)	0.9(0.6)	0.2(0.1)	0.18(0.09)	D
745209.868	161.0	891.6	–	–	≤0.3	≤0.3	ND
1024443.025	295.1	1223.1	–	–	≤0.2	≤0.2	ND

**Notes.** (1)–(3) Spectroscopic line parameters (see references listed in Table 2) of the observed transitions. (4)–(7) Observed line parameters: velocity, linewidth, peak temperature and integrated intensities. The 3σ uncertainties that result from gaussian fits performed with the CLASS software are given in brackets. (8) D: Detected above the 3σ level and ∫T<sub>MB</sub>dV ≥ 5σ, W: Weak line (∫T<sub>MB</sub>dV ≥ 5σ), ND: Not Detected lines (T<sub>MB</sub> < 3σ and ∫T<sub>MB</sub>dV < 5σ).

**Table B.8.** Line Parameters for the HCO<sup>+</sup>, H<sup>13</sup>CO<sup>+</sup> and N<sub>2</sub>H<sup>+</sup> transitions observed toward Cep E–mm.

Frequency (MHz) (1)	E <sub>up</sub> (K) (2)	Sμ <sup>2</sup> (D <sup>2</sup> ) (3)	v (km s <sup>-1</sup> ) (4)	Δv <sub>1/2</sub> (km s <sup>-1</sup> ) (5)	T <sub>MB</sub> (K) (6)	∫T <sub>MB</sub> dV (K km s <sup>-1</sup> ) (7)	Comments (8)
HCO <sup>+</sup>							
535061.581	89.9	90.7	-11.22(0.09)	2.6(0.3)	0.7(0.2)	1.9(0.2)	D
713341.228	154.1	120.9	-10.9(0.4)	2.9(0.9)	0.4(0.4)	1.3(0.4)	W
980636.494	282.4	166.2	-11.5(0.2)	0.5(0.5)	0.5(0.5)	0.3(0.2)	TD
1069693.891	333.8	181.3	–	–	≤0.3	≤0.9	ND
H <sup>13</sup> CO <sup>+</sup>							
520459.884	87.4	90.7	–	–	≤0.2	≤0.2	ND
607174.646	116.6	105.8	–	–	≤0.2	≤0.2	ND
780562.812	187.3	136.1	–	–	≤0.2	≤0.2	ND
N <sub>2</sub> H <sup>+</sup>							
558966.503	93.9	669.5	-10.9(0.2)	0.6(0.4)	0.2(0.1)	0.11(0.06)	W
745209.868	161.0	891.6	–	–	≤0.3	≤0.3	ND
1024443.025	295.1	1223.1	–	–	≤0.2	≤0.2	ND

**Notes.** (1)–(3) Spectroscopic line parameters (see references listed in Table 2) of the observed transitions. (4)–(7) Observed line parameters: velocity, linewidth, peak temperature and integrated intensities. The 3σ uncertainties that result from gaussian fits performed with the CLASS software are given in brackets. (8) D: Detected above the 3σ level and ∫T<sub>MB</sub>dV ≥ 5σ, W: Weak line (∫T<sub>MB</sub>dV ≥ 5σ), ND: Not Detected lines (T<sub>MB</sub> < 3σ and ∫T<sub>MB</sub>dV < 5σ) and, TD: Tentative Detection (line that emits at the 3σ).

**Table B.9.** Line Parameters for the HCO<sup>+</sup>, H<sup>13</sup>CO<sup>+</sup> and N<sub>2</sub>H<sup>+</sup> transitions observed toward NGC7129–FIRS2.

Frequency (MHz) (1)	E <sub>up</sub> (K) (2)	Sμ <sup>2</sup> (D <sup>2</sup> ) (3)	v (km s <sup>-1</sup> ) (4)	Δv <sub>1/2</sub> (km s <sup>-1</sup> ) (5)	T <sub>MB</sub> (K) (6)	∫T <sub>MB</sub> dV (K km s <sup>-1</sup> ) (7)	Comments (8)
HCO <sup>+</sup>							
535061.581	89.9	90.7	-9.7(0.1)	2.5(0.5)	0.46(0.09)	1.2(0.2)	D
713341.228	154.1	120.9	-9.9(0.6)	4.8(1.6)	0.3(0.4)	1.6(0.4)	W
980636.494	282.4	166.2	-10.1(0.7)	2.8(1.5)	0.2(0.4)	0.5(0.3)	W
1069693.891	333.8	181.3	–	–	–	–	NO
H <sup>13</sup> CO <sup>+</sup>							
520459.884	87.4	90.7	–	–	≤0.2	≤0.5	ND
607174.646	116.6	105.8	–	–	≤0.2	≤0.5	ND
780562.812	187.3	136.1	–	–	≤0.1	≤0.4	ND
N <sub>2</sub> H <sup>+</sup>							
558966.503	93.9	669.5	-9.8(0.2)	1.9(0.6)	0.2(0.1)	0.34(0.09)	D
745209.868	161.0	891.6	–	–	≤0.3	≤0.6	ND
1024443.025	295.1	1223.1	–	–	≤0.2	≤0.4	ND

**Notes.** (1)–(3) Spectroscopic line parameters (see references listed in Table 2) of the observed transitions. (4)–(7) Observed line parameters: velocity, linewidth, peak temperature and integrated intensities. The 3σ uncertainties that result from gaussian fits performed with the CLASS software are given in brackets. (8) D: Detected above the 3σ level and ∫T<sub>MB</sub>dV ≥ 5σ, ND: Not Detected lines (T<sub>MB</sub> < 3σ and ∫T<sub>MB</sub>dV < 5σ), W: Weak line (∫T<sub>MB</sub>dV ≥ 5σ), NO: Not observed.